



Net radiative effect of dust aerosols from satellite measurements over Sahara

Eun-Su Yang,¹ Pawan Gupta,¹ and Sundar A. Christopher^{1,2}

Received 26 June 2009; revised 24 August 2009; accepted 31 August 2009; published 29 September 2009.

[1] The clear-sky aerosol top of atmosphere shortwave (SW) and longwave (LW) radiative effects over the Saharan desert (15–30°N, 10°W–30°E) are investigated based entirely on the satellite observations of aerosol optical thickness (AOT), surface albedo, surface temperature, surface emissivity, atmospheric water vapor content, and SW/LW fluxes. The Ozone Monitoring Instrument (OMI) on Aura and the Multi-angle SpectroRadiometer (MISR) on Terra satellite are used to estimate AOT at 558 nm (EAOT) for June to September, 2005–2006 when the predominant aerosol type is dust. We then use these EAOT values in conjunction with broadband measurements from the Clouds and the Earth's Radiant Energy System (CERES) to calculate the top-of-atmosphere SW and LW flux radiative effect due to these aerosols. The difference in SW flux between desert surface and dust aerosols is found to be negligible due to the high surface reflectance over the Sahara desert. The instantaneous area-averaged LW radiative effect is calculated as $+11.4 \text{ Wm}^{-2}$ with radiative efficiencies ranging from +11 to $+26 \text{ Wm}^{-2}/\text{AOT}$. The results indicate that net radiative effect of dust over the Sahara desert is dominated by the longwave effect in contrast to oceans where the shortwave effect dominates. **Citation:** Yang, E.-S., P. Gupta, and S. A. Christopher (2009), Net radiative effect of dust aerosols from satellite measurements over Sahara, *Geophys. Res. Lett.*, 36, L18812, doi:10.1029/2009GL039801.

1. Introduction

[2] Significant advances have been made in the understanding of aerosols and their impact on climate largely due to improved observations and numerical modeling capabilities [e.g., Yu *et al.*, 2006; Schulz *et al.*, 2006]. Global observations of aerosols are now available from multiple sensors that have allowed for studies on aerosol effects on climate, hydrology, air pollution, and health related effects [Kaufman *et al.*, 2002]. Combining information from these sensors provides value added information that is not possible from single sensors alone [Gupta *et al.*, 2008].

[3] Since the study on aerosol impacts requires accurate spatial distribution of aerosols, space-borne sensors use information from the ultraviolet (UV) to the visible and thermal infrared parts of the spectrum to provide global maps of aerosol distribution. Once aerosols are identified, radiative

transfer calculations are used with a priori information about aerosol properties to retrieve aerosol optical thickness (AOT, usually at 550 nm). Several satellite products now exist over desert surfaces such as MIL2ASAE from MISR [Kahn *et al.*, 2005], Deep Blue from MODIS [Hsu *et al.*, 2006], OMAERUV from OMI [Torres *et al.*, 2007], OMAERO from OMI multi-spectral algorithm [Curier *et al.*, 2008], and POLDER [Herman *et al.*, 1997]. However, we do not use these data sets since our aim is not to compare or to evaluate aerosol products. Our goal is mainly to obtain the spatial distribution of AOT to assess aerosol radiative effects. A satellite AOT product such as MISR provides extremely robust retrievals over bright targets [e.g., Christopher and Wang, 2004; Frank *et al.*, 2007] but precludes daily observations due to its narrow swath width. In order to take advantage of the OMI UV Aerosol Index (UVAI) data whose daily values are available for the entire study region, UVAI is converted into AOT values using relationships between OMI UVAI and MISR AOT.

[4] After obtaining the AOT from the OMI UVAI – MISR AOT relationships, we collocate the estimated AOT with the CERES radiative flux data set to quantify the change in top-of-atmosphere (TOA) shortwave (SW) and longwave (LW) flux. From an observational view point, there have been relatively few studies on SW and LW direct radiative effects over the Sahara desert because AOT retrievals over very bright targets are not reliable. This study is first in that the clear-sky SW radiative effect over the center of the Sahara desert is obtained from satellite-based AOT and TOA flux as a function of satellite-based surface albedo. The previous works have performed transport model calculations to produce AOT over bright surfaces or used radiative transfer models to compute SW radiative effects over the Sahara desert [e.g., U.S. Climate Change Science Program, 2009, Figure 2.12, and references therein]. This study also empirically estimates the clear-sky LW flux dependence on surface temperature, surface emissivity, and atmospheric water vapor content, where the dependence was expressed only by radiative transfer models [e.g., Zhang and Christopher, 2003].

2. Data and Methods

[5] There have been significant advances in development of satellite data products over bright surface reflectance regions such as deserts [Hsu *et al.*, 2006; Herman *et al.*, 1997; Torres *et al.*, 2007; Curier *et al.*, 2008]. Multi-sensor methods using MISR-OMI [Christopher *et al.*, 2008] are also useful for estimating AOT over desert regions although they may not be suitable for global applications like those being developed by various science teams. The basic idea is

¹Earth System Science Center, University of Alabama in Huntsville, Huntsville, Alabama, USA.

²Department of Atmospheric Sciences, University of Alabama in Huntsville, Huntsville, Alabama, USA.

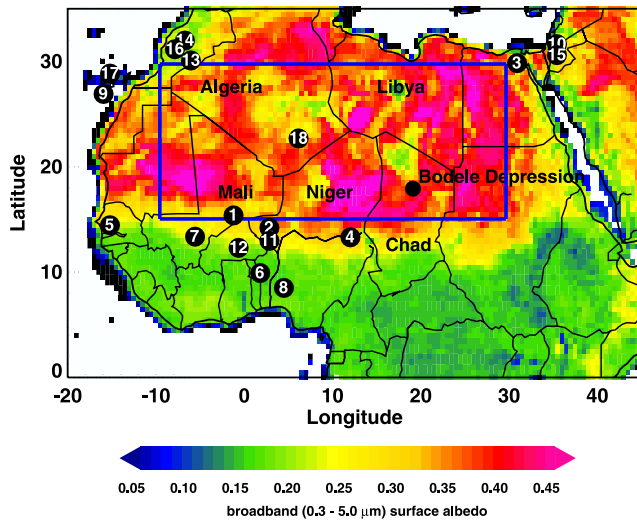


Figure 1. Area of study with MODIS surface albedo. The shaded in color represents the SW white-sky albedo averaged from MCD43C3 for June–September 2005. The area enclosed with blue box is considered to examine direct aerosol radiative forcing. The numbers 1 through 18 are AERONET stations whose names are shown in Figure 3. The Bedele Depression, which is one of a key dust source in the Sahara desert, is shown in northern Chad.

to combine advantages of a reliable MISR AOT product over desert regions (level 2, spatial resolution of $17.6 \times 17.6 \text{ km}^2$ at nadir) with OMI providing a daily coverage of UVAI (level 2, spatial resolution of $13 \times 24 \text{ km}^2$ at nadir). First the MISR AOT is regressed spatially and temporally with the OMI UVAI. These regression relationships are then used to predict AOT from OMI AI values that we call estimated AOT (EAOT). To ensure that the EAOTs are correct, we compare these against AERONET locations. Finally these EAOT's are collocated with the CERES SW and LW fluxes to calculate the TOA radiative impacts.

[6] The AERONET is a global network of sunphotometers that has become the ‘golden standard’ for validating satellite retrievals [Holben *et al.*, 1998]. AERONET uses multiple channels from the UV to near-IR wavelengths to provide columnar AOT and other aerosol property retrievals. We use the level 2 data where the stated AOT accuracies are within ± 0.02 for short wavelengths [Smirnov, 2000].

[7] Since the Saharan surface is inhomogeneous, we used the MODerate-resolution Imaging Spectroradiometer (MODIS) albedo product (MCD43C3) [Schaaf *et al.*, 2002] to characterize the CERES SW flux as a function of surface reflectance. This product provides both directional hemispherical reflectance (black-sky albedo) and bihemispherical reflectance (white-sky albedo) data. MCD43C3 is 16-day composites of observations from MODIS on both Terra and Aqua satellites with a resolution of 0.05 degree. We adjust the grid size to $0.5^\circ \times 0.5^\circ$ to match that of the OMI data used in this study.

[8] The area of study with AERONET locations are shown in Figure 1. Superimposed on Figure 1 is SW white-sky albedo obtained from the MODIS albedo product, where the white-sky albedo is the fraction of incoming diffuse solar radiation reflected back to the atmosphere and space. The

surface albedo shows considerable spatial variability while the whole study area is classified as desert in the IGBP classification.

[9] The CERES instruments provide radiometric measurements of the Earth's atmosphere from three broadband channels ($0.3\text{--}0.5 \mu\text{m}$ for shortwave channel, $8\text{--}12 \mu\text{m}$ for infrared window channel, and $0.3\text{--}200 \mu\text{m}$ for total channel). We use the Single Scanner Footprint (SSF) TOA upward fluxes obtained from Terra and Aqua. Clear-sky data are used where clear area percent coverage is above 99.9% [e.g., Zhang and Christopher, 2003]. The surface emissivity, surface skin temperature, and precipitable water are also adapted from the CERES SSF data set.

3. Estimating AOT From OMI AI Using MISR

[10] In order to take advantage of the OMI UVAI data whose daily values are available for the entire study region, UVAI is converted into AOT values using relationships between OMI UVAI and MISR AOT. Figure 2 shows the relationships between OMI UVAI and MISR AOT in a $10^\circ \times 10^\circ$ grid box. The correlation coefficients between OMI UVAI and MISR AOT are between 0.70 and 0.85 over the desert. See Christopher *et al.* [2008] on the advantages and disadvantages of this method. The daily MISR AOTs and daily OMI UVAI retrievals are calculated for each $0.5^\circ \times 0.5^\circ$ grid cell. Then the MISR AOTs are regressed against the coincident OMI UVAI (~ 3 hours apart from each other) to obtain α (y-intercept) and β (slope) estimates within the $10^\circ \times 10^\circ$ box centered at each grid cell,

$$[\text{MISR AOT}] = \alpha + \beta[\text{UVAI}] \quad (1)$$

The AOT value at 558 nm (EAOT) is estimated from UVAI and α and β in equation (1) for each grid cell by moving the $10^\circ \times 10^\circ$ box,

$$[\text{EAOT}] = \alpha + \beta[\text{UVAI}]. \quad (2)$$

Figure 3 shows a comparison of the EAOT with the AERONET-derived AOT at 558 nm. For coincidence criteria, the AERONET AOT is selected if each AERONET measurement occurs within ± 30 minutes of the OMI measurement and the EAOT is selected if the measurement occurs within $\pm 0.75^\circ$ of the AERONET sites. These

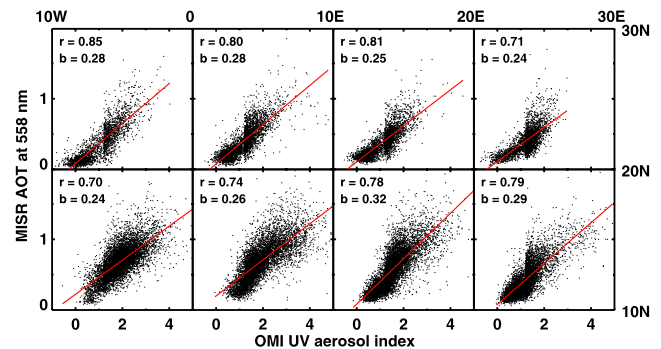


Figure 2. Scatterplots of OMI UVAI versus MISR AOT in $10^\circ \times 10^\circ$ grid box over the area of study for June–September (2005–2006). The correlation coefficient (r) and slope (b) are shown in each plot.

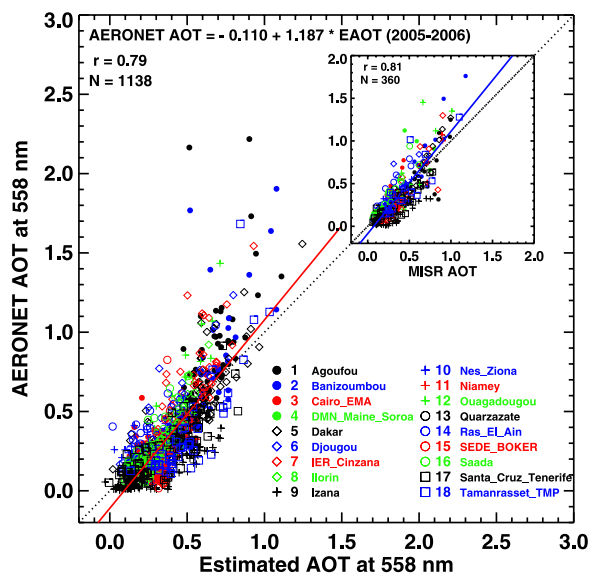


Figure 3. Scatterplot of EAOT (from the OMI AI–MISR AOT relationships) versus AERONET AOT at 558 nm for the period June–September 2005–2006. The slope of the regression line (solid red) is compared with the one-to-one line (dotted black). The name and number of each AERONET station corresponds to the number of station in Figure 1. The inset shows the instantaneous MISR AOT comparison against the AERONET.

coincident AERONET AOT and EAOT show correlation coefficient of 0.79 which provides confidence in the EAOT over the desert region. All available data from the AERONET stations in Figure 1 are included for comparison because mineral dust dominates the region during June to September. Also note that in Figure 3 the EAOT values are systematically high for the EAOT < 0.2 and systematically low for the EAOT > 1.0 compared to the AERONET AOT values. Since there are relatively very few data for EAOT < 0.2 and EAOT > 1.0, these biases do not affect the overall estimate of aerosol radiative effects. The inset shows the instantaneous MISR AOT comparisons with AERONET and as confirms the results of *Christopher et al.* [2008].

4. Aerosol Radiative Effects on TOA SW/LW CERES Fluxes

[11] Once the spatial distribution of aerosols are obtained we use the CERES SW and LW fluxes to examine the change in TOA radiative fluxes between clear and aerosol regions that is called dust radiative effect [e.g., *Zhang and Christopher, 2003*]. We use an empirical approach to separate TOA aerosol radiative effects from flux changes in response to surface and atmospheric properties. In particular, the flux perturbations due to different aerosol and cloud properties are minimized by selecting only the Sahara desert where mineral dust aerosols are dominant (10°W–30°E and 15–30°N, blue box in Figure 1) and by using only cloud-free CERES flux data. Furthermore using EAOTs derived from OMI provides about 200,000 of AOT-flux pairs, which are enough to divide the physical parameters representing surface and atmospheric properties into narrow ranges of

their values. For example, EAOTs are divided into 16 bins from 0.0 to 1.5 with an increment of 0.1 to represent different aerosol loadings. Similar but smaller numbers of bins are produced for surface albedo (α_s), surface skin temperature (T_s), surface emissivity (ϵ_s), and atmospheric water content (P_w). TOA SW flux is largely a function of surface reflectivity and aerosol properties [*Ackerman and Chung, 1992*] whereas the TOA LW flux is affected by water vapor content and surface thermal emission which in turn depends on atmospheric and surface conditions [*Zhang and Christopher, 2003*]. Due to the relatively large size, the dust aerosols can effectively absorb outgoing terrestrial radiation from the surface and re-emit at higher altitudes and cold temperatures, leading to warming of the Earth and therefore a positive TOA longwave forcing.

[12] In order to obtain aerosol-only signal imbedded in TOA SW and LW flux, the effect of these parameters should be separated, that has been shown in radiative modeling approaches as flux changes with AOT at fixed α_s , T_s , ϵ_s , P_w , and so on [*Fu and Liou, 1993; Zhang and Christopher, 2003*]. The number of parameters can be reduced by combining surface skin temperature and surface emissivity, which leads to surface thermal emittance ($\epsilon_s T_s^4$). The change in TOA SW fluxes are examined by changing EAOT for each surface albedo bin width of 0.02. Similarly, the change in TOA LW fluxes are examined by changing EAOT for each surface thermal emittance bin width of 0.5 and atmospheric water content bin width of 1.0.

[13] The TOA SW and LW radiative effect (SWRE and LWRE) are defined as $F_{\text{clear}} - F_{\text{aerosol}}$ [e.g., *Christopher and Zhang, 2002*], where F_{clear} and F_{aerosol} are the TOA SW and LW flux observed in clear and aerosol conditions. The radiative efficiency is also defined as $(F_{\text{clear}} - F_{\text{aerosol}})/\text{AOT}$. Note that SWRE and LWRE are positive if there is a warming influence. Figure 4a shows the SW flux increases as surface albedo (α_s) increases, but does not change much at fixed values of α_s . The range of EAOT also increases with the surface albedo, for example, from 0.1 to 0.7 at $\alpha_s = 0.20$ and from 0.1 to 1.3 at $\alpha_s = 0.40$. If the effect of changing α_s were not adequately separated by several subintervals, the SW fluxes would have shown a larger variance with AOT. The slope of AOT versus SW flux, which represents radiative effect, would also have been erroneously positive because high AOT occurs more often in the areas with high SW flux. The large variance and sampling bias problems are now reduced by showing the SW flux change within a narrow range of α_s . In Figure 4a, the SWRE appears insignificant in the Sahara desert (the average and standard deviation are estimated as $1.6 \pm 11.3 \text{ Wm}^{-2}$ over the study area), which was also noted by *Hsu et al.* [2000] and *Patadia et al.* [2009]. A careful inspection of Figure 4a reveals that the aerosol SW radiative efficiency is slightly negative (cooling influence) at α_s below 0.32 and near zero or slightly positive at α_s above 0.36.

[14] The TOA LW flux is shown in Figure 4b as a function of the surface thermal emittance and atmospheric water vapor content, where the surface temperature is normalized to surface temperature of 300 K ($\epsilon_s [T_s/300]^4$). The TOA flux increases with increasing surface thermal emittance and with decreasing P_w . There is a clear dependence of LW flux on AOT when atmospheric water content is low ($P_w = 1.0$ and 2.0 gcm^{-2}). The instantaneous LWRE

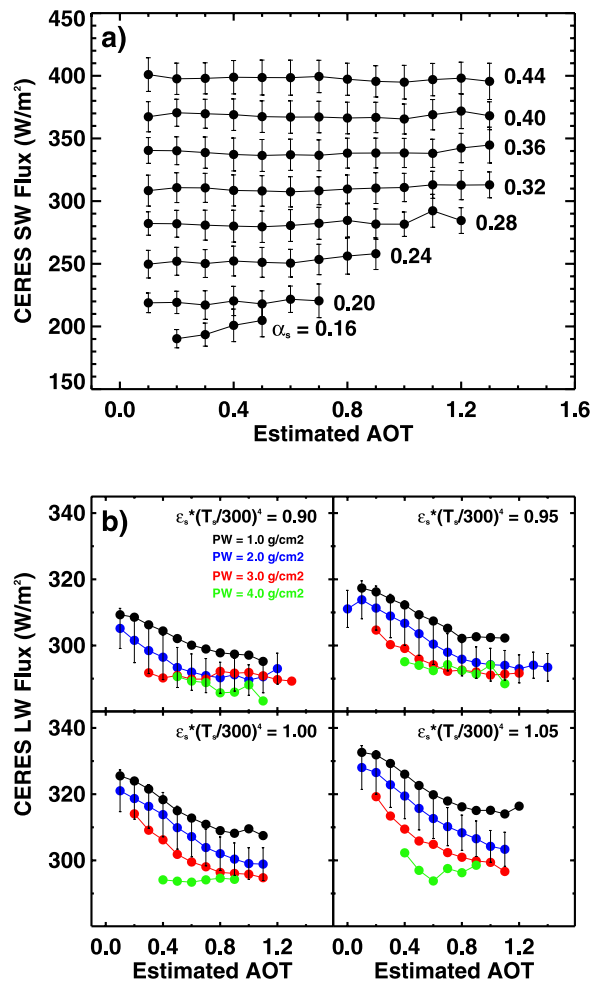


Figure 4. (a) Estimated AOT versus TOA SW flux as a function of surface albedo for the Sahara desert region. The vertical bar represents the 1-sigma standard deviation from the mean flux in each AOT bin. The surface albedo is presented with numeric characters. (b) Estimated AOT versus TOA LW flux as a function of surface thermal emittance and atmospheric water content for the Sahara desert region. The surface thermal emittance is normalized to the surface temperature of 300 K. The atmospheric water content is presented with numeric characters in unit of g cm^{-2} . The standard error bars for the LW fluxes are shown for water content of 2.0 g cm^{-2} .

averaged over the study area is $+11.4 \pm 7.2 \text{ W m}^{-2}$, comparable to 7 W m^{-2} reported by Zhang and Christopher [2003]. The aerosol LW radiative efficiencies range from 11 to $26 \text{ W m}^{-2}/\text{AOT}$ at $P_w = 1.0$ and 2.0 g cm^{-2} . The efficiency is estimated as $+24.3 \pm 1.3 \text{ W m}^{-2}/\text{AOT}$ at typical values of $P_w = 2.0$ and $\epsilon_s^* [T_s/300]^4 = 1.0$ over the study area during summer. This radiative efficiency is comparable to the results of Zhang and Christopher [2003].

5. Summary and Discussion

[15] Dust AOT is estimated by using the relationship between OMI UVAI and MISR AOT at 558 nm. Converting daily OMI AI to AOT significantly improves spatial and

temporal coverage of AOT over the Saharan desert, which cannot be achieved from the sparse sampling of MISR AOT. Good agreements are found between the estimated AOT and AERONET AOT. Using EAOT, we examine the relations between AOT and TOA CERES SW and LW fluxes. By confining surface and atmospheric parameters into a small range, the surface and atmospheric contributions to SW and LW fluxes are separated. The variations in SW flux are mostly explained by the spatial difference of surface reflectivity over the desert. It is shown that the SW flux change is not statistically significant with increasing AOT within a small range (± 0.01) of surface albedo. This is expected over the Saharan desert because the difference in reflectivity between the bright surface (area-averaged $\alpha_s = 0.40$) and the aerosol layer is insignificant. However, due to their large particle sizes and the colder temperature at which dust aerosols emit, there is a significant difference in TOA upward LW flux between the surface and dust layers thereby causing a warming effect. The area-averaged LW radiative forcing and its efficiency are estimated as $+11.4 \text{ W m}^{-2}$ and $+11$ to $+26 \text{ W m}^{-2}/\text{AOT}$ at $P_w = 1.0$ and 2.0 g cm^{-2} , that are comparable to the previous results [Zhang and Christopher, 2003]. The net radiative effect over the Sahara is dominated entirely by the longwave over deserts. In contrast, over oceans the longwave effect accounts for only 20% of the shortwave effect [Christopher and Jones, 2007].

[16] **Acknowledgments.** This research is supported by NASA's Radiation sciences, Interdisciplinary sciences, and ACPMAP programs. The data were obtained through the NASA Langley Distributed Active Archive Center.

References

- Ackerman, S. A., and H. Chung (1992), Radiative effects of airborne dust on regional energy budgets at the top of the atmosphere, *J. Appl. Meteorol.*, **31**, 223–233, doi:10.1175/1520-0450(1992)031<0223:REOADO>2.0.CO;2.
- U.S. Climate Change Science Program (2009), Atmospheric aerosol properties and climate impacts: A report by the U.S. Climate Change Science Program and the Subcommittee on Global Change Research, edited by M. Chin et al., 128 pp., NASA, Washington, D. C.
- Christopher, S. A., and T. Jones (2007), Satellite-based assessment of cloud-free net radiative effect of dust aerosols over the Atlantic Ocean, *Geophys. Res. Lett.*, **34**, L02810, doi:10.1029/2006GL027783.
- Christopher, S. A., and J. Wang (2004), Intercomparison between MISR and Sunphotometer AOT in dust source regions over China: Implication for satellite retrievals and radiative forcing calculations, *Tellus, Ser. B*, **56**(5), 451–456, doi:10.1111/j.1600-0889.2004.00120.x.
- Christopher, S. A., and J. Zhang (2002), Shortwave aerosol radiative forcing from MODIS and CERES observations over the oceans, *Geophys. Res. Lett.*, **29**(18), 1859, doi:10.1029/2002GL014803.
- Christopher, S. A., P. Gupta, J. Haywood, and G. Greed (2008), Aerosol optical thicknesses over North Africa: 1. Development of a product for model validation using Ozone Monitoring Instrument, Multiangle Imaging Spectroradiometer, and Aerosol Robotic Network, *J. Geophys. Res.*, **113**, D00C04, doi:10.1029/2007JD009446.
- Curier, R. L., J. P. Veefkind, R. Braak, B. Veihelmann, O. Torres, and G. de Leeuw (2008), Retrieval of aerosol optical properties from OMI radiances using a multiwavelength algorithm: Application to western Europe, *J. Geophys. Res.*, **113**, D17S90, doi:10.1029/2007JD008738.
- Frank, T. D., et al. (2007), The spatial and temporal variability of aerosol optical depths in the Mojave Desert of southern California, *Remote Sens. Environ.*, **107**, 54–64, doi:10.1016/j.rse.2006.06.024.
- Fu, Q., and K. N. Liou (1993), Parameterization of the radiative properties of cirrus clouds, *J. Atmos. Sci.*, **50**, 2008–2025, doi:10.1175/1520-0469(1993)050<2008:POTRPO>2.0.CO;2.
- Gupta, P., F. Patadia, and S. A. Christopher (2008), Multi-sensor data product fusion for aerosol research, *IEEE Trans. Geosci. Remote Sens.*, **46**, 1407–1415, doi:10.1109/TGRS.2008.916087.
- Herman, M., J. L. Deuze, C. Devaux, P. Goloub, F. M. Breonand, and D. Tanré (1997), Remote sensing of aerosols over land surfaces including

- polarization measurements and application to POLDER measurements, *J. Geophys. Res.*, *102*, 17,039–17,049, doi:10.1029/96JD02109.
- Holben, B. N., et al. (1998), A federated instrument network and data archive for aerosol characterization, *Remote Sens. Environ.*, *66*, 1–16, doi:10.1016/S0034-4257(98)00031-5.
- Hsu, N. C., J. R. Herman, and C. Weaver (2000), Determination of radiative forcing of Saharan dust using combined TOMS and ERBE data, *J. Geophys. Res.*, *105*, 20,649–20,662, doi:10.1029/2000JD900150.
- Hsu, N. C., S. C. Tsay, M. D. King, and J. R. Herman (2006), Deep blue retrievals of Asian aerosol properties during ACE-Asia, *IEEE Trans. Geosci. Remote Sens.*, *44*, 3180–3195, doi:10.1109/TGRS.2006.879540.
- Kahn, R. A., B. J. Gaitley, J. V. Martonchik, D. J. Diner, K. A. Crean, and B. Holben (2005), Multiangle Imaging Spectroradiometer (MISR) global aerosol optical depth validation based on 2 years of coincident Aerosol Robotic Network (AERONET) observations, *J. Geophys. Res.*, *110*, D10S04, doi:10.1029/2004JD004706.
- Kaufman, Y. J., D. Tanré, and O. Boucher (2002), A satellite view of aerosols in the 5 climate system, *Nature*, *419*, 215–223, doi:10.1038/nature01091.
- Patadia, F., E.-S. Yang, and S. A. Christopher (2009), Does dust change the clear sky top of atmosphere shortwave flux over high surface reflectance regions?, *Geophys. Res. Lett.*, *36*, L15825, doi:10.1029/2009GL039092.
- Schaaf, C. B., et al. (2002), First operational BRDF, albedo nadir reflectance products from MODIS, *Remote Sens. Environ.*, *83*, 135–148, doi:10.1016/S0034-4257(02)00091-3.
- Schulz, M., et al. (2006), Radiative forcing by aerosols as derived from the AeroCom present-day and pre-industrial simulations, *Atmos. Chem. Phys.*, *6*, 5225–5246.
- Smirnov, A. (2000), Cloud-screening and quality control algorithms for the AERONET database, *Remote Sens. Environ.*, *73*, 337–349, doi:10.1016/S0034-4257(00)00109-7.
- Torres, O., A. Tanskanen, B. Veihelmann, C. Ahn, R. Braak, P. K. Bhartia, P. Veeffkind, and P. Levelt (2007), Aerosols and surface UV products from Ozone Monitoring Instrument observations: An overview, *J. Geophys. Res.*, *112*, D24S47, doi:10.1029/2007JD008809.
- Yu, H., et al. (2006), A review of measurement-based assessments of the aerosol direct radiative effect and forcing, *Atmos. Chem. Phys.*, *6*, 613–666.
- Zhang, J., and S. A. Christopher (2003), Longwave radiative forcing of dust aerosols over the Saharan Desert estimated from MODIS, MISR, and CERES observations from Terra, *Geophys. Res. Lett.*, *30*(23), 2188, doi:10.1029/2003GL018479.

S. A. Christopher, Department of Atmospheric Sciences, University of Alabama in Huntsville, 320 Sparkman Drive, Huntsville, AL 35806-1912, USA.

P. Gupta and E.-S. Yang, Earth System Science Center, University of Alabama in Huntsville, 320 Sparkman Drive, Huntsville, AL 35806-1912, USA. (yes@nsstc.uah.edu)